Journal of Materials Chemistry A

PAPER

View Article Online
View Journal | View Issue

Cite this: J. Mater. Chem. A, 2019, 7, 6920

Hybrid chemical vapor deposition enables scalable and stable Cs-FA mixed cation perovskite solar modules with a designated area of 91.8 cm^2 approaching 10% efficiency†

Longbin Qiu, ‡[a] Sisi He, ‡[a] Yan Jiang, [a] Dae-Yong Son, [a] Luis K. Ono, [a] Zonghao Liu, [a] Taehoon Kim, [a] Theodoros Bouloumis, [a] Said Kazaoui [b] and Yabing Qi *[a]

The development of scalable deposition methods for stable perovskite layers is a prerequisite for the development and future commercialization of perovskite solar modules. However, there are two major challenges, *i.e.*, scalability and stability. In sharp contrast to a previous report, here we develop a fully vapor based scalable hybrid chemical vapor deposition (HCVD) process for depositing Cs-formamidinium (FA) mixed cation perovskite films, which alleviates the problem encountered when using conventional solution coating of mainly methylammonium lead iodide ($MAPbI_3$). Using our HCVD method, we fabricate perovskite films of $Cs_{0.1}FA_{0.9}PbI_{2.9}Br_{0.1}$ with enhanced thermal and phase stabilities, by the intimate incorporation of Cs into FA based perovskite films. In addition, the SnO_2 electron transport layer (ETL) (prepared by sputter deposition) is found to be damaged during the HCVD process. In combination with precise interface engineering of the SnO_2 ETL, we demonstrate relatively large area solar modules with efficiency approaching 10% and with a designated area of 91.8 cm^2 fabricated on 10 cm × 10 cm substrates (14 cells in series). On the basis of our preliminary operational stability tests on encapsulated perovskite solar modules, we extrapolated that the T_{80} lifetime is approximately 500 h (under the light illumination of 1 sun and 25 °C).

Received 8th January 2019
Accepted 18th February 2019

DOI: 10.1039/c9ta00239a

rsc.li/materials-a

Introduction

The development of perovskite solar cells/modules remains unprecedented with a certified stabilized output efficiency of 20.9% for small cells (0.991 cm^2), 17.25% for mini-modules (17.277 cm^2) and 11.7% for submodules (703 cm^2).[1] However, there are still two main challenges to be addressed, namely scalability and stability.[2] As a general trend that can be learned from other photovoltaic technologies (Si and CdTe), the absolute efficiency decay with scaling up the area is estimated to be approximately 0.8% per decade.[3] Hence, when a 1 cm^2 solar cell with 20% efficiency is scaled up to a solar module of 100 cm^2 designated area, the efficiency is expected to be 18.4%, according to the estimated decay rate. However, at the current stage the published results in the literature indicate that for perovskite solar cell devices the efficiency decays much faster upon scaling up the area.[3]

This can be explained by mainly two causes. First, the decay in the efficiency would be influenced by perovskite deposition methods. So far the most efficient perovskite solar cells are processed by the spin-coating method and reported on small active areas, *e.g.*, from approximately 0.1 cm^2 to 1 cm^2. A high quality perovskite film is easily obtained on this area.[4] However, the film quality deteriorates as the film size increases to a typical solar module size, *i.e.*, 100 cm^2.[2,3] It is thus necessary to develop perovskite deposition methods capable of depositing large area films with high quality.[5] Currently, scalable solution coating methods including spray coating, slot-die coating and doctor blading are under rapid development. Large area methylammonium lead iodide ($MAPbI_3$) modules up to 45 cm × 65 cm have been demonstrated in a previous study.[6] However, this coating method is less efficient than the spin coating in small cells. Furthermore, volatile solvents are not environmentally friendly. Besides solution coating methods, efforts have been made in utilizing vapor deposition for perovskite solar cells/modules, owing to its advantages of conformal coating over large area, elimination of toxic solvents, precise film thickness control, and outstanding compatibility with

[a]Energy Materials and Surface Sciences Unit (EMSSU), Okinawa Institute of Science and Technology Graduate University (OIST), 1919-1 Tancha, Onna-son, Kunigami-gun, Okinawa 904-0495, Japan. E-mail: Yabing.Qi@OIST.jp

[b]Research Center for Photovoltaics (RCPV), National Institute of Advanced Industrial Science and Technology (AIST), Tsukuba, Ibaraki 305-8565, Japan

† Electronic supplementary information (ESI) available. See DOI: 10.1039/c9ta00239a

‡ L. Qiu and S. He contributed equally to this work.

tandem solar cell fabrication.[7] For example, a hybrid chemical vapor deposition (HCVD) process was developed to fabricate $MAPbI_3$ and formamidinium lead iodide ($FAPbI_3$) based solar modules.[8] In this process, perovskite films are formed in two steps. In the first step, a lead halide film such as PbI_2, $PbCl_2$ or $PbBr_2$ is deposited by thermal evaporation. In the second step, the as prepared lead halide film is reacted with organic halide species under a controlled vapor atmosphere and pressure to form perovskite films inside a tube furnace. The composition of the perovskite can be readily tuned by changing the organic vapor atmosphere, from MAI to FAI or MABr, to obtain $MAPbI_3$, $FAPbI_3$ or $MAPbBr_3$, respectively.[9] With the controllable deposition of perovskite, HCVD is promising for large scale fabrication of high performance/stable perovskite solar cells and light emitting diodes.[9] Second, the rapid decay in efficiency can also originate from the nonoptimal module design (non-ohmic interconnection contact between FTO/Au leading to high series resistance and large dead area due to P1, P2, P3 patterning). A likely cause responsible for the faster efficiency decay upon scaling up of area comes from the transparent conducting electrode sheet resistance, which often leads to reduction in the fill factor.[10] The module design of stripes in series connection is a solution that can significantly increase the aspect ratio of each sub-cell and reduce the resistance effect. The maximum stripe width is limited by the transparent conducting electrode sheet resistance.[11] In this design, the relation between stripe width and transparent conducting electrode sheet resistance should be considered, as for each stripe there will be an area for making interconnection, which is a dead area. A strategy to reduce resistance is to pattern narrower stripes. However, this will also lead to a lower active area to total area ratio, *i.e.*, a lower geometric fill factor (GFF). In addition, using mask-patterning instead of other finely controlled patterning techniques such as laser scribing or mechanical scribing results in a GFF as low as 50%, at the early stage of the perovskite solar module design.[8,12] On the basis of calculation results, for highly conductive FTO substrates (10 $\Omega\ \square^{-1}$), the stripe width could be up to 7 mm with a small dead area to reach the maximum power output.[10] A GFF as high as 95% has been demonstrated by using the laser patterning technique and it offers a better design for active area approaching the total area of the substrate.[13]

Although the number of reports on perovskite solar modules is increasing gradually, they are mainly based on solution coated $MAPbI_3$.[2] With modified precursor solution properties by adding surfactant, large area, 57.2 cm^2, solar modules with doctor blading $MAPbI_3$ have been fabricated with an efficiency up to 14.6%.[14] In another study, by adding excess MACl to the $MAPbI_3$ precursor ink, a high quality film has been deposited by blade coating and the module with an area of 12.6 cm^2 showed an efficiency of 13.3%.[15] The efficiency was further improved to 15.6% with $MA_{0.7}FA_{0.3}PbI_3$ and interconnection optimization.[16] From an intermediate design of $PbI_2 \cdot nMA$ and $MAI \cdot mMA$ precursors, a solvent- and vacuum-free tape assisted coating process has been developed for $MAPbI_3$ based modules, with a certified efficiency of 12.1% on an area of 36.1 cm^2.[5] A slot-die coated perovskite solar module with an area up to 168.75 cm^2 was also based on $MAPbI_3$, with the efficiency reaching 10%.[17] Another aspect to be considered is the operational lifetime. Although the area and efficiency are increasing with research efforts, $MAPbI_3$ is not suitable for commercialization, due to its instability under heat, light, humidity and oxygen.[18] A new trend in the field is to employ thermally more stable FA based mixed cation (especially Cs cations) perovskites to improve stability.[19] In FA based mixed cation perovskites, a small amount of Cs could stabilize the perovskite phase leading to both high performance and stable perovskite solar modules.[20] In addition, with the Cs concentration in the range of 10–30%, charge-carrier mobility, charge-carrier lifetime and crystal quality are substantially improved.[21] A few studies reported the solution coating of Cs containing FA based perovskite solar cells; however, very few studies reported with solar modules.[2,22] Our group previously reported the successful fabrication of mini-modules with a $Cs_{0.07}FA_{0.93}PbI_3$ perovskite utilizing a cation exchange process.[23] These mini-modules showed high stability under continuous light illumination. A recent work reported the fabrication of $Cs_xFA_{1-x}PbI_{3-y}Br_y$ based perovskite solar modules using a vapor–solid reaction method that could be considered as a combination of physical vapor deposition and low pressure chemical vapor deposition.[24] We would like to stress that these reported modules present a relatively modest GFFs, and relative small active areas (12 cm^2 on a 5 cm × 5 cm substrate, with 6 cells in series,[23] and 41.25 cm^2 on an 8 cm × 8 cm substrate, with 9 cells in series[24]). Further scale up of FA based mixed cation perovskites with large area and also a high GFF is important for the development of perovskite solar modules.

Here we show the scalability of the HCVD process in deposition of FA-Cs based mixed perovskites for stable large area solar modules on 10 cm × 10 cm substrates with a high GFF (>90%). This fully vapor based process eliminates the use of toxic solvents such as dimethylformamide and dimethyl sulfoxide, which are not environmentally friendly. The composition of the perovskite layer could be readily changed from $MAPbI_3$ to $FAPbI_3$ and FA-Cs mixed cation perovskite, by controlling the precursor composition during the HCVD process. With co-evaporation of CsBr and PbI_2 in the first step, followed by exposure to FAI vapor in the second step, we successfully fabricated a Cs-FA perovskite, $Cs_{0.1}FA_{0.9}PbI_{2.9}Br_{0.1}$, through a fully vapor based process. We also find that one critical issue for HCVD perovskite solar cells/modules is the vacuum annealing process which might damage the SnO_2 layer. A C_{60} layer with a thickness of 5 nm was inserted between SnO_2 and perovskite, which would passivate and modulate the energy levels at these interfaces. Benefiting from the fully vapor based HCVD process, the film and interface showed little difference between small area cells and large area modules. With the area increasing by 1000-fold from 0.09 cm^2 to 91.8 cm^2, we demonstrate that the device's designated area PCE decreases slightly (from 13.3% to 9.34%, which corresponds to a PCE drop of 1.3% per decade), suggesting that this fully vapor based vacuum deposition process is a promising route towards scalability. In addition, the HCVD method is promising because it allows the synthesis of a relatively stable perovskite composition such as $Cs_{0.1}FA_{0.9}PbI_{2.9}Br_{0.1}$. The

operational lifetime of these encapsulated glass/FTO/SnO_2/C_{60}/perovskite/spiro-MeOTAD/Au/Parylene/glass solar modules was studied, which showed an extrapolated T_{80} lifetime of approximately 500 h under one sun continuous illumination and steady state power output.

Results and discussion

Hybrid chemical vapor deposition

Fig. 1 displays the fully vapor based HCVD process for the fabrication of perovskite films with controlled compositions. The perovskite formation proceeds in two steps as we previously developed.[9] The first step (Fig. 1a) is slightly modified, with the vacuum co-evaporation of inorganic precursors including PbI_2 and CsBr. The intended composition in this work is 10% Cs and 90% FA cations, considering a suitable band-gap for single junction solar cells, phase stability, and high quality.[21] A small amount of Br is incorporated to further improve the perovskite stability.[25] Although a layer-by-layer deposition of CsBr and PbI_2 might help precisely control the thickness of each layer,[26] after the HCVD process, the resulting film will have a gradient composition structure because the interdiffusion of CsBr and PbI_2 (both are much less volatile than FAI) during the HCVD process is expected to be much slower than that of FAI. Based on such consideration, we employed co-evaporation in this work to ensure a uniform distribution of the CsBr–PbI_2 mixed film. To achieve 10% Cs, the evaporation rates of PbI_2 and CsBr are controlled to be 0.10 nm s^{-1} and 0.01 nm s^{-1}, respectively. The deposition rate and thickness of the co-evaporated film are monitored using a quartz crystal microbalance (QCM). The thickness of the co-evaporated PbI_2/CsBr film is approximately 185 nm. In the second step (Fig. 1b), the PbI_2/CsBr coated substrate is transferred to a multi-zone tube furnace with the FAI organic precursor in the upstream side and the substrates placed in the downstream side. Upon exposure to FAI vapor and at 150 °C, the PbI_2/CsBr film readily converts into the $Cs_{0.1}FA_{0.9}PbI_{2.9}Br_{0.1}$ perovskite film. As shown in Fig. 1c and d, the yellow co-evaporated PbI_2/CsBr film and the dark brown $Cs_{0.1}FA_{0.9}PbI_{2.9}Br_{0.1}$ perovskite film are uniformly coated on a stripe-patterned FTO substrate, with a size of 10 cm × 10 cm. These results demonstrate the excellent apparent uniformity of the as-prepared $Cs_{0.1}FA_{0.9}PbI_{2.9}Br_{0.1}$ perovskite film.

The microstructure of the co-evaporated PbI_2/CsBr film and $Cs_{0.1}FA_{0.9}PbI_{2.9}Br_{0.1}$ perovskite film after HCVD is further studied (Fig. 2). The cross-section image of the co-evaporated PbI_2/CsBr film on top of FTO confirms that the PbI_2/CsBr film consists of nano-plates with high roughness (Fig. 2a and c). The thickness of this PbI_2/CsBr layer is expected to be 185 nm, monitored using a QCM during the thermal evaporation. However, due to the rough surface as shown in Fig. 2a, it is difficult to determine the thickness accurately. After the HCVD

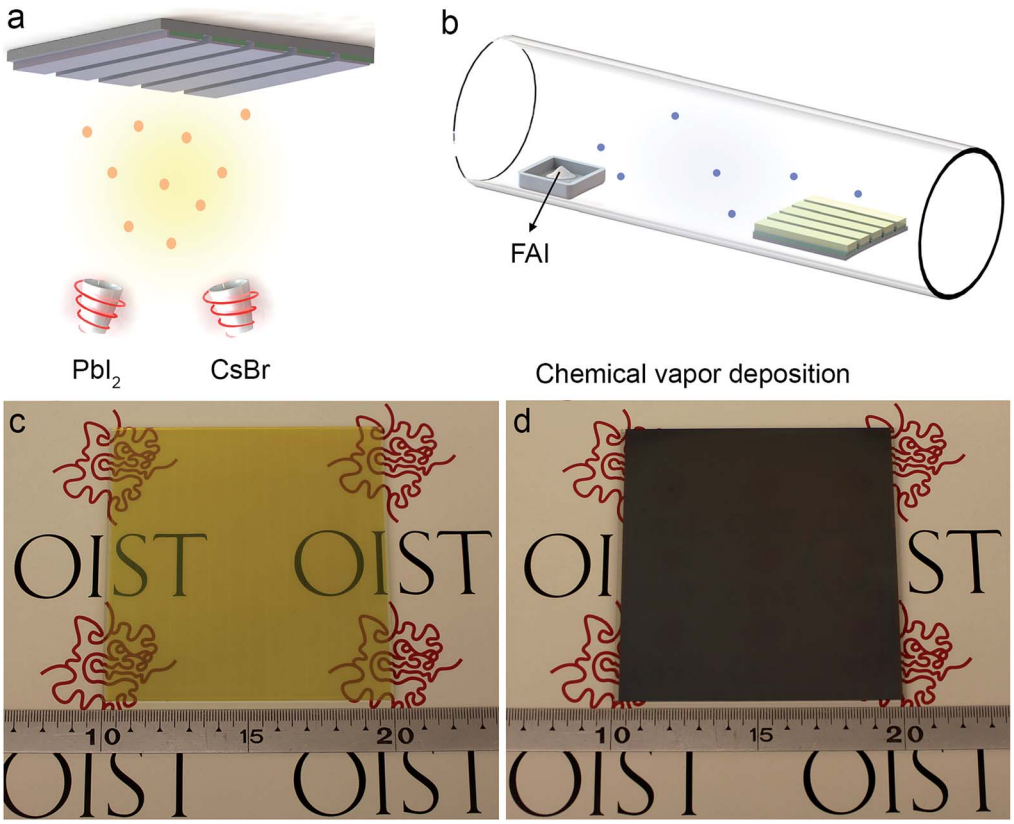

Fig. 1 Schematic drawing showing the HCVD process. (a) Thermal evaporation of inorganic precursors including PbI_2 and CsBr. (b) HCVD of the FAI organic precursor for the formation of perovskite. Optical images of (c) the co-evaporated PbI_2/CsBr film and (d) the HCVD $Cs_{0.1}FA_{0.9}PbI_{2.9}Br_{0.1}$ perovskite film (96 cm^2 on a 100 cm^2 patterned FTO substrate).

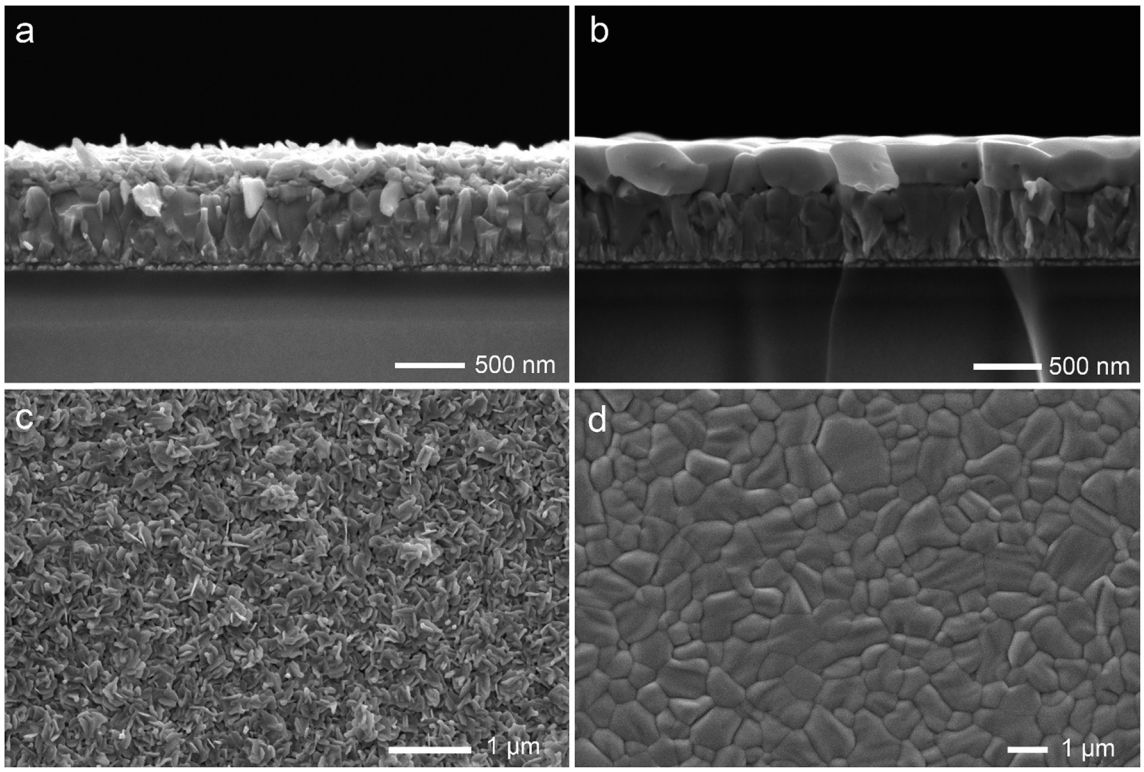

Fig. 2 Microstructure of PbI_2/CsBr before and after HCVD. Cross-section SEM image of (a) PbI_2/CsBr and (b) $Cs_{0.1}FA_{0.9}PbI_{2.9}Br_{0.1}$ perovskite films. Surface SEM image of (c) PbI_2/CsBr and (d) $Cs_{0.1}FA_{0.9}PbI_{2.9}Br_{0.1}$ perovskite films.

process with the FAI vapor, the perovskite film thickness is approximately 400 nm (Fig. 2b), and the perovskite film is characterized by large grains and an ultra-smooth surface (Fig. 2d). The film thickness after the HCVD process is found to increase by a factor of 2.16. The thickness increase of the fully converted perovskite film could be estimated from the density of PbI_2 (6.16 g cm^{-3}) and $FAPbI_3$ (4.10 g cm^{-3}).[9b,27] With the assumption of full conversion and exclusion of the small amount of Cs, the expected thickness would increase by a factor of 2.03, which is in good agreement with the cross-section SEM images (Fig. 2b). These results confirm the excellent uniformity of the as-prepared $Cs_{0.1}FA_{0.9}PbI_{2.9}Br_{0.1}$ perovskite film.

The crystal structure and composition of the HCVD deposited $Cs_{0.1}FA_{0.9}PbI_{2.9}Br_{0.1}$ perovskite film were further characterized. In Fig. 3a, the (110) perovskite peak at 13.99° is clearly observed without any residual PbI_2 signal at 12.6° after HCVD (inset in Fig. 3a), which confirms that FAI could diffuse to the bottom and completely react with the PbI_2/CsBr film. Furthermore, no diffraction peaks appear at 11.7° corresponding to the non-perovskite phase of $FAPbI_3$, suggesting good phase purity of the $Cs_{0.1}FA_{0.9}PbI_{2.9}Br_{0.1}$ perovskite films prepared by HCVD. The optical absorbance edge of the perovskite film is 798 nm (Fig. 3b), which corresponds to an optical band of 1.56 eV from a Tauc-plot (Fig. S1†). To study the composition of the perovskite film, X-ray photoelectron spectroscopy (XPS) is performed (Table S1†). Before and after HCVD, the ratio between Cs and Pb is approximately 0.1, which is consistent with the deposition rate monitored using a QCM (Fig. 3c and d). After HCVD, the intensity of Br 3d signal is weaker (Fig. 3e).[28] Regarding the decreased Br 3d signal, whether this is because there is phase separation on the top surface or the Br actually evaporates after the HCVD process is currently under further investigation. The XPS mapping further confirms the uniform distribution of Cs and Br in the perovskite layer (Fig. S2†). To confirm the composition, a $Cs_{0.1}FA_{0.9}PbI_{2.9}Br_{0.1}$ film made by a solution coating process was prepared and compared with $Cs_{0.1}FA_{0.9}PbI_{2.9}Br_{0.1}$ made by HCVD.[25] As shown in Fig. S3 and S4,† the XRD and UV-vis absorbance of $Cs_{0.1}FA_{0.9}PbI_{2.9}Br_{0.1}$ synthesized by solution and HCVD methods are very similar and thus we infer that their compositions are also similar. The reaction of PbI_2/CsBr with FAI and annealing at ~150 °C seem to relatively decrease the concentration of Br on the top surface of the perovskite (Fig. S5†). The core level of N 1s is ascribed to FA cations, which also indicates the incorporation of FAI for the perovskite formation (Fig. 3f).

Small area solar cells

The carrier lifetime of $Cs_{0.1}FA_{0.9}PbI_{2.9}Br_{0.1}$ on bare glass made by HCVD was investigated by time-resolved photoluminescence (TRPL), as presented in Fig. S6.† The upper limit of the open-circuit voltage (V_{OC}) due to the non-radiative recombination in the perovskite is calculated to be approximately 1.04 V at room temperature (ESI note 1†).[11,29] Further study is necessary to improve the film quality and to reduce the defect density to achieve long carrier lifetime.[30] To check the photovoltaic performance of this HCVD deposited $Cs_{0.1}FA_{0.9}PbI_{2.9}Br_{0.1}$ film,

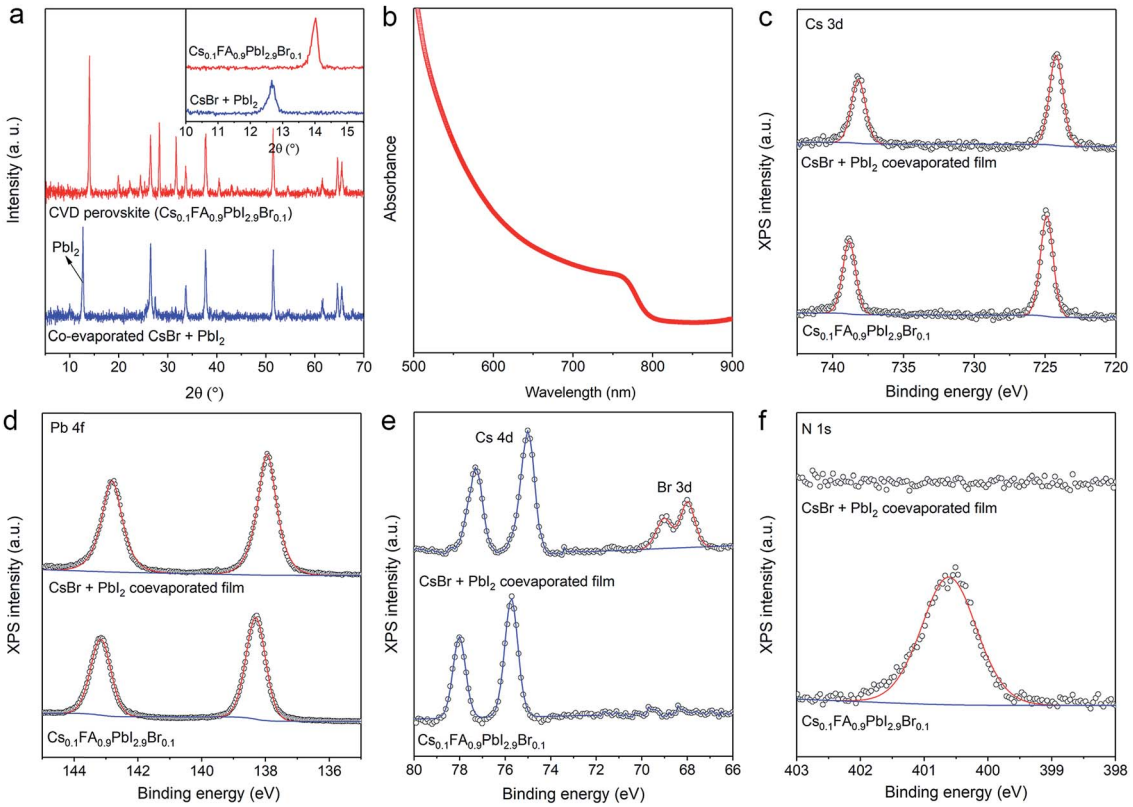

Fig. 3 Structure and composition of the HCVD perovskite layer. (a) XRD before and after HCVD, which indicate a high quality perovskite structure. (b) Optical absorbance of $Cs_{0.1}FA_{0.9}PbI_{2.9}Br_{0.1}$. XPS core levels of (c) Cs 3d, (d) Pb 4f, (e) Cs 4d and Br 3d and (f) N 1s before and after HCVD, which indicate the formation of $Cs_{0.1}FA_{0.9}PbI_{2.9}Br_{0.1}$.

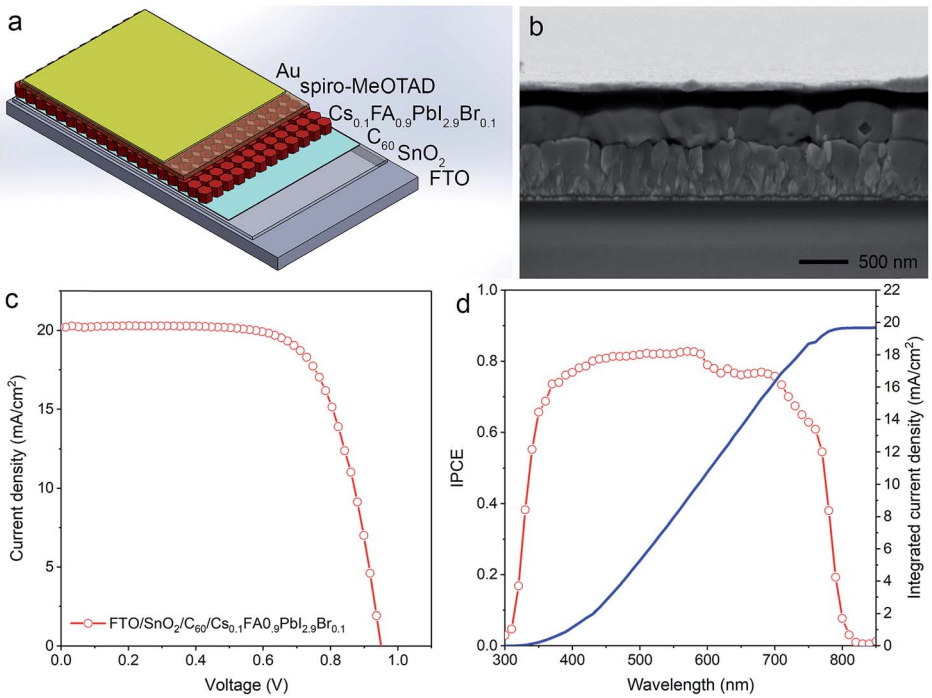

Fig. 4 $Cs_{0.1}FA_{0.9}PbI_{2.9}Br_{0.1}$ based planar junction solar cell performance. (a) Schematic drawing showing the planar junction device structure. (b) Cross-section SEM image of the HCVD $Cs_{0.1}FA_{0.9}PbI_{2.9}Br_{0.1}$ based solar cell. Typical (c) *J*–*V* curve and (d) IPCE spectra of HCVD $Cs_{0.1}FA_{0.9}PbI_{2.9}Br_{0.1}$ based solar cells.

a planar junction structured device was applied with sputtered SnO_2 as the electron transport layer (ETL) (Fig. 4a). The sputtered SnO_2 film was optimized according to our recent work and achieves an efficiency over 20% based on spin coated perovskite films.[31] However, the HCVD device's performance is lower than expected. As shown in Fig. S7,† from the typical *J–V* curves of the solar cells, the average V_{OC} value is 0.81 V (Table S2†), which is much lower than the calculated upper limit due to the non-radiative recombination (1.04 V). We find that the vacuum annealing process during HCVD damages the SnO_2 layer. Ultraviolet photoemission spectroscopy (UPS) and XPS measurements of the SnO_2 layer before and after the vacuum annealing process were performed to study the gap states (Fig. S8†). These states are believed to be mainly caused by oxygen deficiency after vacuum annealing (Fig. S9†). These gap states after the vacuum annealing process lower the hole-blocking properties of the SnO_2 ETL.[31,32] To confirm the effect of the vacuum annealing process, a control experiment was performed. Solution processed devices were fabricated on sputtered SnO_2 with and without the vacuum annealing process. As shown in Table S3 and Fig. S10,† the photovoltaic performances of solution coated perovskite solar cells on sputtered SnO_2 with and without the vacuum annealing process differ significantly. After vacuum annealing the performance of SnO_2 degrades significantly, and all the device photovoltaic parameters decrease. Especially the V_{OC} decreases from 1.03 V to 0.73 V. As a control experiment the effect of vacuum annealing was also studied based on the most used SnO_2 film prepared from Alfa Aesar solution.[33] This crystalline SnO_2 film also shows reduced performance after the vacuum annealing process (Table S3†). This shows that the negative effect induced by vacuum annealing is not limited to sputtered SnO_2 films. Note that this is not unique to SnO_2, because it also occurs for TiO_2 annealed in an inert atmosphere (such as in a N_2 glove box) where oxygen vacancy defects deteriorate the perovskite solar cell's performance.[34]

In this case, SnO_2 surface modification is necessary to achieve a high quality layer for electron extraction and hole blocking. A thin layer of C_{60} was evaporated on top of SnO_2 before co-evaporation of PbI_2/CsBr as a buffer and passivation layer. The energy level diagram from UPS measurement is shown in Fig. S11,† which confirms the smooth transfer of charges across the interface.[35] Regarding the influence on the SnO_2 films induced by vacuum annealing, we further performed a control experiment on a sputtered SnO_2/C_{60} electron transport layer before and after vacuum annealing to study the effect of C_{60} passivation (Table S3†). Note that in the case of "SnO_2/C_{60}", the efficiency with vacuum annealing is only slightly lower than that without vacuum annealing, suggesting that the negative effect of vacuum annealing is largely mitigated by adding a thin film of C_{60} with a thickness of 5 nm. However, when comparing the case of SnO_2/C_{60} with the case of SnO_2 before vacuum annealing, the device efficiency is about 10–20% lower in the case of SnO_2/C_{60}. The factor that might influence the device performance in the case of SnO_2/C_{60} is air exposure during the sample transfer. It has been shown that C_{60} has poor air stability, which may induce oxygen-trap states and decrease charge carrier lifetime.[36] Air exposure after C_{60} deposition is proposed to be the main reason for the lower performance. With this vacuum deposited SnO_2/C_{60} bilayer as the ETL, solar cells based on perovskite $Cs_{0.1}FA_{0.9}PbI_{2.9}Br_{0.1}$ made by HCVD were fabricated with the structure glass/FTO/SnO_2/C_{60}/perovskite/spiro-MeOTAD/Au (Fig. 4a). A clear layer-by-layer structure of the planar junction device can be observed in the cross-section SEM image (Fig. 4b). The active layer thickness is around 400 nm. With this planar junction structure the champion small cell efficiency is 13.3% (0.09 cm^2). Improving the perovskite's optoelectronic quality and engineering the perovskite and ETL interfaces to reduce the non-radiative carrier recombination rates at bulk and interfaces are possible strategies to further boost the solar cell's performance. As shown in Fig. 4c, from the typical *J–V* curve of solar cells with HCVD $Cs_{0.1}FA_{0.9}PbI_{2.9}Br_{0.1}$, the average V_{OC} is 0.90 V (Table S2†). The short circuit current density (J_{SC}) is around 20.2 mA cm^{-2}, which is consistent with IPCE spectra (Fig. 4d). Currently, the average fill factor is around 0.67 leaving room for further improvement.

Large area solar modules

The deposition process is very promising for large scale solar module fabrication. The scale-up of the $Cs_{0.1}FA_{0.9}PbI_{2.9}Br_{0.1}$ solar cells to 10 cm × 10 cm solar modules through the HCVD method is further demonstrated (Fig. 5a). The module comprises 14 sub-cells connected in series. For each FTO stripe, the width is 6.6 mm, with 0.1 mm P1 patterning in between each FTO stripe. The length of the stripe is 98 mm resulting in an area of 6.468 cm^2 for each stripe. The interconnection area is formed by CO_2 laser scribing, with a width around 0.15 mm (P2). Finally, mechanical scribing is used to separate each sub-cell by forming a P3 patterning (0.05 mm). The P1–P2–P3 patterning is shown in Fig. S12.† Considering the FTO stripe width plus P1 width (6.7 mm) and the dead area for sub-cell series connection (0.68 mm), the geometric fill factor is up to 90%. 10 solar modules were fabricated, and the photovoltaic parameters of which are listed in Table S4.† The plot for the champion solar module is shown in Fig. 5b. The modules were further encapsulated by deposition of a Parylene film[37] on top of the Au electrode and then a cover glass was sealed on top with UV-curable glue on the edges to further prevent water and oxygen infiltration as well as to ensure good thermal contact with the cooling stage to dissipate heat (Fig. S13†). This low temperature encapsulation process does not affect the module's performance (Fig. S14†). The best performance is 9.34% with a designated area of 91.8 cm^2 (Fig. 5b) and the active area efficiency reaches 10.37% (active area = 82.6 cm^2).

With a GFF of 90%, the short-circuit current (I_{SC}) is expected to be 119 mA considering the J_{SC} value obtained from the small cell (20.2 mA cm^{-2}) and the area of each cell stripe (5.909 cm^2). Indeed, the measured I_{SC} from solar modules is mostly around 110 mA (Table S4†), which clearly demonstrates the success of our fine patterning process and the scalability of our HCVD method. The average V_{OC} for modules is 12.8 V and for each sub-cell is 0.91 V. The V_{OC} of sub-cells in the modules also matches well with the values obtained for the small area cells (Tables S2

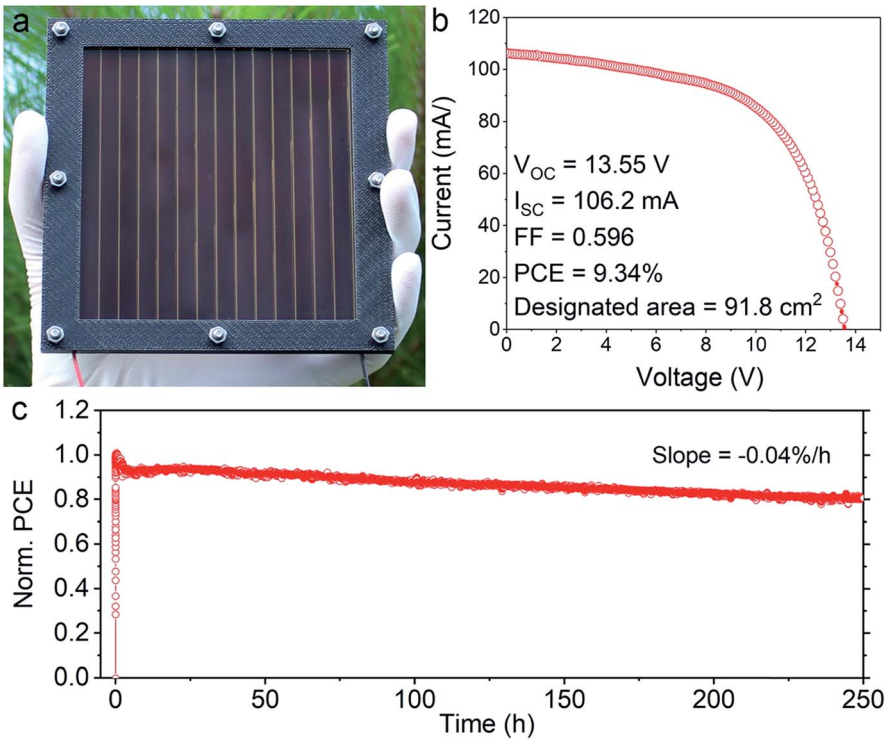

Fig. 5 $Cs_{0.1}FA_{0.9}PbI_{2.9}Br_{0.1}$ based solar module performance. (a) Optical image of a 10 cm × 10 cm HCVD $Cs_{0.1}FA_{0.9}PbI_{2.9}Br_{0.1}$ based solar module. (b) *J*–*V* curve of the champion 10 cm × 10 cm HCVD $Cs_{0.1}FA_{0.9}PbI_{2.9}Br_{0.1}$ based solar module (14 sub-cells in series). (c) Operational stability of the HCVD solar module under one-sun illumination and steady-state power output tracking.

and S4†). From the small area cells to modules, the area is enlarged over 1000 times (from 0.09 cm^2 to 91.8 cm^2). The champion efficiency decreased from 13.3% to 9.3% (active area efficiency 10.4%) (Fig. S15†), which is only slightly lower than expected (10.9%) if assuming an efficiency-against-area decay rate of 0.8% per decade. The decrease mainly comes from the lower fill factor. Without removing the bottom SnO_2 layer (17 nm), the contact resistance might also increase compared with the Au/FTO interface contact resistance, which might be the main cause for the lower fill factor.[38] This module shows hysteresis with a hysteresis factor around 0.17 (hysteresis factor = $(PCE_{Reverse} - PCE_{Forward})/PCE_{Reverse}$) (Fig. S16†),[39] and needs further engineering of the interface and perovskite composition.[33,39] As a demonstration of the broad composition adjustment of perovskites by HCVD, the same 10 cm × 10 cm sized modules but with a $MAPbI_3$ active layer were fabricated. The performance is lower than that of the $Cs_{0.1}FA_{0.9}PbI_{2.9}Br_{0.1}$ based solar modules (Fig. S17†), due to the mismatch of the energy level alignment as shown in Fig. S11.† This demonstrates the scalability of our HCVD method for large area monolithic perovskite solar modules, with desired composition.

The HCVD method for mixed cation perovskite is promising for achieving stable solar modules. Here the operational lifetime is measured with encapsulated 5 cm × 5 cm mini-modules with a designated area of 22.4 cm^2. The module consists of 7 cells connected in series and exhibits a designated area efficiency around 10%, which is consistent with a decay rate of 1.3% per decade (Fig. S15 and S18†). The operational lifetime was measured under a controlled temperature of 25 °C and continuous one sun illumination with steady state power output. From Fig. 5c we can first observe a burn-in loss of power output within approximately the first ten hours with 90% of its initial performance remaining.[40] A slow decay of the performance with a slope of −0.04% h^{-1} follows after the burn-in loss, which corresponds to a T_{80} lifetime of 500 h.[41] These results demonstrate the good long-term stability of the $Cs_{0.1}FA_{0.9}PbI_{2.9}Br_{0.1}$ based solar module produced through our HCVD method.

Conclusions

In summary, with the mixed-cation Cs-FA based perovskite films deposited by HCVD, a SnO_2/C_{60} ETL deposited by sputtering and thermal evaporation, and a Parylene encapsulation layer deposited by chemical vapor deposition, fully scalable perovskite solar modules with 91.8 cm^2 designated area on 100 cm^2 substrates are developed. Based on the fully vapor based deposition process there is no limitation for the module area and the absolute efficiency decay is consistent with that of other commercialized photovoltaic techniques when scaling-up. The operational T_{80} lifetime under illumination is extrapolated to be approximately 500 h. With further interface engineering and perovskite film post-treatment, the device performance could be improved. We believe that HCVD will be a strong tool for progressing towards commercialization of perovskite photovoltaics.

Experimental

HCVD

The HCVD process is performed in a multi-zone tube furnace with solid FAI powder as the precursor. The FAI powder is first converted to the gas phase in the upstream zone when heated up to 190 °C. With the assistance of a low flux of carrier gas (air with a relative humidity of 45% in this case; flux = 60 sccm), the gas phase FAI is driven uniformly towards the downstream zone where the chemical reaction takes place between FAI and the pre-deposited $CsBr/PbI_2$ substrate. The other end of the tube furnace is connected to a pump, which results in an overall average vacuum level of approximately 1 torr in the furnace. The temperature of the downstream zone is approximately 150 °C. The pressure at the end with the input carrier gas is expected to be slightly higher and gradually decreases towards the end connected to the pump. The gentle gradient of pressure along the tube serves as the driving force to move the FAI vapor from one end to the other. During HCVD, the FAI powder source is abundant, therefore for the first order approximation we can consider the FAI concentration in the gas stream to be constant along the tube, if we do not take into account the slight decrease of the FAI concentration down the stream due to a small amount of FAI reacting with the $CsBr/PbI_2$ substrates. According to the equation $D_g \propto T^{3/2}/P$ (where D_g is the diffusion constant, T is the temperature, and P is the pressure),[9b] the diffusion rate of gas phase FAI to the substrate is approximately constant. Also, the adsorption rate of FAI on the substrate can be assumed to be constant and independent (or only has a weak dependence) of the deposited film's thickness. As a result, the film thickness of the deposited FAI is determined by the total deposition time and will be uniform across the entire length of the tube furnace.

Solar cell/module fabrication

Patterned FTO glass with a sheet resistance around 7 $\Omega\ \square^{-1}$ (OPVT) was first ultrasonically washed sequentially with 1 wt% sodium dodecyl sulfate aqueous, de-ionized water, acetone and isopropanol for 15 min. The dry FTO substrate was then sputtered coated with 17 nm SnO_2 and evaporated with 5 nm C_{60}, with a deposition rate of 0.7 nm min^{-1} and 0.02 nm s^{-1}, respectively. The perovskite active layer was deposited by a HCVD process developed in our early work,[8,9] with different precursor compositions. PbI_2 and CsBr were thermally co-evaporated on a C_{60} coated FTO/SnO_2 substrate with a rate of 0.10 nm s^{-1} and 0.01 nm s^{-1}, respectively, for 185 nm. The PbI_2/CsBr coated substrate was then transferred to a multi-zone tube furnace. The Cs salt is sensitive to water. To avoid the moisture effect, the tube furnace was quickly pumped down to 1 torr after loading the $CsBr/PbI_2$ substrate. The FAI vapor was carried by air with a relative humidity of 45%. The mixed O_2/N_2 carrier gas helps passivate shallow and deep traps in the converted perovskite film.[42] On the other hand, with such a low pressure level of air (1 torr) and the substrate temperature at approximately 150 °C, we expect the moisture in the carrier gas to have a minimal negative impact on the final perovskite film.[43] After reaction and cooling, the perovskite film was washed with saturated potassium iodide solution (isopropanol) and annealed at 100 °C for 20 min. A hole transport material solution containing 29 mg spiro-MeOTAD, 11.5 μL TBP, and 7 μL Li-TFSI solution (520 mg mL^{-1} in acetonitrile) in 0.4 mL chlorobenzene was spin coated on top of the perovskite layer. For the solar module the P2 patterning was performed using a CO_2 laser with a power of 5.6 W. At the end, 120 nm Au was thermally evaporated as the back contact electrode and each sub-cell was separated by mechanical scribing to form P3 patterning. The solar modules were encapsulated by 2 μm thick chemical vapor deposited Parylene and sealed using a cover glass with a thickness of 2 mm. This Parylene film was reported to be resistant to water.[37]

Characterization

The absorbance spectra of the perovskite were recorded with a UV-vis spectrometer (Jasco V-670). The ultraviolet photoemission spectroscopy (UPS) and X-ray photoelectron spectroscopy (XPS) spectra were recorded using an XPS-AXIS Ultra HAS (Kratos) equipped with monochromatic Al-Kα = 1486.6 eV and non-monochromatic He-I = 21.22 eV sources. Sample damage induced by UV and X-ray was monitored by taking five consecutive scans. Surface morphology and cross-section characterization were performed using a scanning electron microscope (FEI Quanta 250 FEG). The crystal structure of the perovskite was measured using an X-ray diffractometer (XRD) (Bruker D8 Discover). Time resolved photoluminescence (TRPL) spectra of the perovskite film on bare glass were acquired using the time-correlated, single-photon counting technique (Hamamatsu, C10627), and excitation was provided by a femtosecond mode-locked Ti:sapphire laser (SpectraPhysics, MAITAI XF-IMW) at 450 nm. *J–V* curves of the solar cells/modules were recorded using a Keithley 2420 Source Meter. The simulated AM1.5 solar light comes from a solar simulator (Oriel-Sol1A equipped with a 450 W Xe lamp and an AM1.5 filter), with an illumination intensity of 100 mW cm^{-2} calibrated using a reference Si solar cell. The designated area of 0.09 cm^2 for small cells, 22.4 cm^2 for small modules and 91.8 cm^2 for large modules were defined by a corresponding metal mask. For solar cell/module characterization, the dwell time is 10 ms, for small cells in the range of −0.1 V to 1.2 V, 5 cm × 5 cm modules in the range of −0.1 V to 7.0 V and 10 cm × 10 cm modules in the range of −1 V to 14.0 V. The EQE spectra of small cells were characterized using Oriel IQE 200.

Conflicts of interest

There are no conflicts to declare.

Acknowledgements

This work was supported by funding from the Energy Materials and Surface Sciences Unit of the Okinawa Institute of Science and Technology Graduate University, the OIST Proof of Concept (POC) Program, the OIST R&D Cluster Research Program, and JSPS KAKENHI Grant Number JP18K05266. We would like to

thank OIST Mech. Eng. & Microfabrication Support Section for maintenance of cleanroom and sputtering equipment.

Notes and references

1 M. A. Green, Y. Hishikawa, E. D. Dunlop, D. H. Levi, J. Hohl-Ebinger, M. Yoshita and A. W. Y. Ho-Baillie, *Prog. Photovoltaics Res. Appl.*, 2019, **27**, 3.
2 L. Qiu, L. K. Ono and Y. B. Qi, *Materials Today Energy*, 2018, **7**, 169.
3 Z. Li, T. R. Klein, D. H. Kim, M. Yang, J. J. Berry, M. F. A. M. van Hest and K. Zhu, *Nat. Rev. Mater.*, 2018, **3**, 18017.
4 W. S. Yang, B.-W. Park, E. H. Jung, N. J. Jeon, Y. C. Kim, D. U. Lee, S. S. Shin, J. Seo, E. K. Kim, J. H. Noh and S. I. Seok, *Science*, 2017, **356**, 1376.
5 H. Chen, F. Ye, W. Tang, J. He, M. Yin, Y. Wang, F. Xie, E. Bi, X. Yang, M. Grätzel and L. Han, *Nature*, 2017, **550**, 92.
6 C. Longhua, L. Lusheng, W. Jifeng, D. Bin, G. Lili and F. Bin, *J. Semiconduct.*, 2017, **38**, 014006.
7 (*a*) L. K. Ono, M. R. Leyden, S. Wang and Y. B. Qi, *J. Mater. Chem. A*, 2016, **4**, 6693; (*b*) O. Malinkiewicz, A. Yella, Y. H. Lee, G. M. Espallargas, M. Graetzel, M. K. Nazeeruddin and H. J. Bolink, *Nat. Photonics*, 2014, **8**, 128; (*c*) D. Perez-del-Rey, P. P. Boix, M. Sessolo, A. Hadipour and H. J. Bolink, *J. Phys. Chem. Lett.*, 2018, **9**, 1041; (*d*) S. Wang, X. Li, J. Wu, W. Wen and Y. B. Qi, *Curr. Opin. Electrochem.*, 2018, **11**, 130.
8 M. R. Leyden, Y. Jiang and Y. B. Qi, *J. Mater. Chem. A*, 2016, **4**, 13125.
9 (*a*) M. R. Leyden, M. V. Lee, S. R. Raga and Y. B. Qi, *J. Mater. Chem. A*, 2015, **3**, 16097; (*b*) M. R. Leyden, L. K. Ono, S. R. Raga, Y. Kato, S. Wang and Y. B. Qi, *J. Mater. Chem. A*, 2014, **2**, 18742; (*c*) M. R. Leyden, L. Meng, Y. Jiang, L. K. Ono, L. Qiu, E. J. Juarez-Perez, C. Qin, C. Adachi and Y. B. Qi, *J. Phys. Chem. Lett.*, 2017, **8**, 3193.
10 M. Stolterfoht, C. M. Wolff, J. A. Márquez, S. Zhang, C. J. Hages, D. Rothhardt, S. Albrecht, P. L. Burn, P. Meredith, T. Unold and D. Neher, *Nat. Energy*, 2018, **3**, 847.
11 Y. Galagan, E. W. C. Coenen, W. J. H. Verhees and R. Andriessen, *J. Mater. Chem. A*, 2016, **4**, 5700.
12 D. H. Kim, J. B. Whitaker, Z. Li, M. F. A. M. van Hest and K. Zhu, *Joule*, 2018, **2**, 1437.
13 A. L. Palma, F. Matteocci, A. Agresti, S. Pescetelli, E. Calabrò, L. Vesce, S. Christiansen, M. Schmidt and A. D. Carlo, *IEEE J. Photovolt.*, 2017, **7**, 1674.
14 Y. Deng, X. Zheng, Y. Bai, Q. Wang, J. Zhao and J. Huang, *Nat. Energy*, 2018, **3**, 560.
15 M. Yang, Z. Li, M. O. Reese, O. G. Reid, D. H. Kim, S. Siol, T. R. Klein, Y. Yan, J. J. Berry, M. F. A. M. van Hest and K. Zhu, *Nat. Energy*, 2017, **2**, 17038.
16 M. Yang, D. H. Kim, T. R. Klein, Z. Li, M. O. Reese, B. J. Tremolet de Villers, J. J. Berry, M. F. A. M. van Hest and K. Zhu, *ACS Energy Lett.*, 2018, **3**, 322.
17 F. Di Giacomo, S. Shanmugam, H. Fledderus, B. J. Bruijnaers, W. J. H. Verhees, M. S. Dorenkamper, S. C. Veenstra, W. Qiu, R. Gehlhaar, T. Merckx, T. Aernouts, R. Andriessen and Y. Galagan, *Sol. Energy Mater. Sol. Cells*, 2018, **181**, 53.
18 (*a*) S. Wang, Y. Jiang, E. J. Juarez-Perez, L. K. Ono and Y. B. Qi, *Nat. Energy*, 2016, **2**, 16195; (*b*) S.-H. Turren-Cruz, A. Hagfeldt and M. Saliba, *Science*, 2018, **362**, 449; (*c*) E. J. Juarez-Perez, Z. Hawash, S. R. Raga, L. K. Ono and Y. B. Qi, *Energy Environ. Sci.*, 2016, **9**, 3406; (*d*) E. J. Juarez-Perez, L. K. Ono, M. Maeda, Y. Jiang, Z. Hawash and Y. B. Qi, *J. Mater. Chem. A*, 2018, **6**, 9604; (*e*) L. K. Ono, Y. B. Qi and S. F. Liu, *Joule*, 2018, **2**, 1961.
19 M. Saliba, T. Matsui, J.-Y. Seo, K. Domanski, J.-P. Correa-Baena, M. K. Nazeeruddin, S. M. Zakeeruddin, W. Tress, A. Abate, A. Hagfeldt and M. Grätzel, *Energy Environ. Sci.*, 2016, **9**, 1989.
20 C. Yi, J. Luo, S. Meloni, A. Boziki, N. Ashari-Astani, C. Grätzel, S. M. Zakeeruddin, U. Röthlisberger and M. Grätzel, *Energy Environ. Sci.*, 2016, **9**, 656.
21 W. Rehman, D. P. McMeekin, J. B. Patel, R. L. Milot, M. B. Johnston, H. J. Snaith and L. M. Herz, *Energy Environ. Sci.*, 2017, **10**, 361.
22 Z. Yang, S. Zhang, L. Li and W. Chen, *J. Mater.*, 2017, **3**, 231.
23 Y. Jiang, M. R. Leyden, L. Qiu, S. Wang, L. K. Ono, Z. Wu, E. J. Juarez-Perez and Y. B. Qi, *Adv. Funct. Mater.*, 2018, **28**, 1703835.
24 L. Luo, Y. Zhang, N. Chai, X. Deng, J. Zhong, F. Huang, Y. Peng, Y.-B. Cheng and Z. Ku, *J. Mater. Chem. A*, 2018, **6**, 21143.
25 H.-S. Yoo and N.-G. Park, *Sol. Energy Mater. Sol. Cells*, 2018, **179**, 57.
26 G. Tong, H. Li, G. Li, T. Zhang, C. Li, L. Yu, J. Xu, Y. Jiang, Y. Shi and K. Chen, *Nano Energy*, 2018, **48**, 536.
27 C. C. Stoumpos, C. D. Malliakas and M. G. Kanatzidis, *Inorg. Chem.*, 2013, **52**, 9019.
28 J. Endres, M. Kulbak, L. Zhan, B. P. Rand, D. Cahen, G. Hodes and A. Kahn, *J. Appl. Phys.*, 2017, **121**, 035304.
29 W. Tress, *Adv. Energy Mater.*, 2017, **7**, 1602358.
30 Z. Liu, L. Qiu, E. J. Juarez-Perez, Z. Hawash, T. Kim, Y. Jiang, Z. Wu, S. R. Raga, L. K. Ono, S. Liu and Y. B. Qi, *Nat. Commun.*, 2018, **9**, 3880.
31 L. Qiu, Z. Liu, L. K. Ono, Y. Jiang, D.-Y. Son, Z. Hawash, S. He and Y. B. Qi, *Adv. Funct. Mater.*, 2018, 1806779, DOI: 10.1002/adfm.201806779.
32 M. Batzill, K. Katsiev, J. M. Burst, U. Diebold, A. M. Chaka and B. Delley, *Phys. Rev. B: Condens. Matter Mater. Phys.*, 2005, **72**, 165414.
33 D. Yang, R. Yang, K. Wang, C. Wu, X. Zhu, J. Feng, X. Ren, G. Fang, S. Priya and S. Liu, *Nat. Commun.*, 2018, **9**, 3239.
34 (*a*) V. Sivaram, E. J. W. Crossland, T. Leijtens, N. K. Noel, J. Alexander-Webber, P. Docampo and H. J. Snaith, *J. Phys. Chem. C*, 2014, **118**, 1821; (*b*) M. Saliba, J.-P. Correa-Baena, C. M. Wolff, M. Stolterfoht, N. Phung, S. Albrecht, D. Neher and A. Abate, *Chem. Mater.*, 2018, **30**, 4193.
35 C. Xiao, C. Wang, W. Ke, B. P. Gorman, J. Ye, C.-S. Jiang, Y. Yan and M. M. Al-Jassim, *ACS Appl. Mater. Interfaces*, 2017, **9**, 38373.

36 J. P. Bastos, E. Voroshazi, E. Fron, G. Brammertz, T. Vangerven, M. V. Auweraer, J. Poortmans and D. Cheyns, *ACS Appl. Mater. Interfaces*, 2016, **8**, 9798.
37 H. Jinno, K. Fukuda, X. Xu, S. Park, Y. Suzuki, M. Koizumi, T. Yokota, I. Osaka, K. Takimiya and T. Someya, *Nat. Energy*, 2017, **2**, 780.
38 F. Matteocci, L. Cinà, F. Di Giacomo, S. Razza, A. L. Palma, A. Guidobaldi, A. D'Epifanio, S. Licoccia, T. M. Brown, A. Reale and A. Di Carlo, *Prog. Photovoltaics Res. Appl.*, 2016, **24**, 436.
39 Z. Tang, T. Bessho, F. Awai, T. Kinoshita, M. M. Maitani, R. Jono, T. N. Murakami, H. Wang, T. Kubo, S. Uchida and H. Segawa, *Sci. Rep.*, 2017, **7**, 12183.
40 J. A. Christians, P. Schulz, J. S. Tinkham, T. H. Schloemer, S. P. Harvey, B. J. Tremolet de Villers, A. Sellinger, J. J. Berry and J. M. Luther, *Nat. Energy*, 2018, **3**, 68.
41 K. Domanski, E. A. Alharbi, A. Hagfeldt, M. Grätzel and W. Tress, *Nat. Energy*, 2018, **3**, 61.
42 A. Ng, Z. Ren, Q. Shen, S. H. Cheung, H. C. Gokkaya, S. K. So, A. B. Djurišić, Y. Wan, X. Wu and C. Surya, *ACS Appl. Mater. Interfaces*, 2016, **8**, 32805.
43 J. Huang, S. Tan, P. D. Lund and H. Zhou, *Energy Environ. Sci.*, 2017, **10**, 2284.